Applied Thermal Engineering 167 (2020) 114778

Contents lists available at ScienceDirect

Applied Thermal Engineering

journal homepage: www.elsevier.com/locate/apthermeng

An experimental study on a hot-air-based anti-/de-icing system for aero-engine inlet guide vanes

Linkai Li[a], Yang Liu[a], Linchuan Tian[a], Haiyang Hu[a], Hui Hu[a,*], Xuejun Liu[b], Isaac Hogate[b], Atul Kohli[b]

[a] Department of Aerospace Engineering, Iowa State University, Ames, IA 50010, USA
[b] Pratt & Whitney, 400 Main Street, East Hartford, CT 06118, USA

HIGHLIGHTS

- A hot-air-based system is evaluated for the icing protection of aero-engine IGVs.
- A novel IGV model with hot-air flowing conduit is developed for the experimental study.
- The physics of icing of IGV is clarified to minimize the use of bleed air as de-icing tool.
- The IGV surface is fully ice free at a hot-air stream T of 30 °C and mass flow rate of 4 g/s.
- Our quantitative measurement results are useful for modeling validation/verification.

ARTICLE INFO

Keywords:
Aero-engine icing physics
Inlet guide vane icing protection
Hot-air-based anti-/de-icing system

ABSTRACT

In the present study, a comprehensive experimental study was conducted to quantify the dynamic ice accretion process on aero-engine inlet guide vanes (IGVs) and to characterize a hot-air-based anti-/de-icing system in order to optimize the design paradigms to reduce the requirements of the bleed air for IGV icing protection, thereby, minimizing the performance penalties to the aero-engines. A hollowed IGV model embedded with U-shaped hot-air flowing conduit was designed/manufactured and mounted inside an Icing Research Tunnel for the experimental study. During the experiments, while a high-speed imaging system was used to record the dynamic ice accretion or anti-/de-icing process over the surface of the IGV model for the test cases without and with turning on the hot-air supply system, the corresponding surface temperature distributions on the IGV model were also measured quantitatively by using a row of embedded thermocouples. The unsteady heat transfer process over the surface of the IGV model was analyzed quantitatively, revealing that the convective heat transfer would dissipate over 85% of the thermal energy provided by the hot-air stream for the anti-/de-icing operation. A comprehensive parametric study was also conducted to evaluate the effects of the operation parameters of the hot-air-based system on its performance for IGV icing protection. It was demonstrated clearly that, with proper operation parameter settings (i.e., the temperature of the hot-air stream being greater than 30 °C and its flow rate is higher than 4.0 g/s), the hot-air-based system was able to effectively prevent ice formation/accretion over the entire IGV surface. The quantitative measurement results would not only be very helpful to elucidate the underlying physics of the important microphysical processes pertinent to IGV icing phenomena, but also can be used as valued database to validate/verify theoretical modeling and numerical simulations for the development of effective and robust anti-/de-icing systems to protect IGVs from harsh icing environment.

1. Introduction

Inlet guide vanes (IGVs), which located between the air intake components and intermediate compressors, are critical components of aero-engines. IGVs are susceptible to direct impingement of super-cooled water droplets with the consequence of possible ice formation/accretion as aero-engines operate in cold weather. Ice accreted over the surfaces of IGVs would not only block the passage of airflow to the compressor but also can shed from IGVs by vibration, heat, or other effects to cause significant foreign object damage (FOD) [1], or even be

* Corresponding author.
E-mail address: huhui@iastate.edu (H. Hu).

https://doi.org/10.1016/j.applthermaleng.2019.114778
Received 1 August 2019; Received in revised form 4 December 2019; Accepted 5 December 2019
Available online 09 December 2019
1359-4311/

sucked into engine core resulting in severe power loss issues, such as stall, surge or even flameout [2].

In order to mitigate the potentially detrimental effects of ice accretion over IGVs on aero-engine performance, an effective anti-/de-icing strategy for IGV icing protection is highly promoted. A number of anti-/de-icing methods have been developed for the icing protection of aero-engine components (e.g., inlet lip, spinner or inlet guide vanes) in recent years, which can be categorized as hot-air-based systems [3–6], hot-oil-based systems [7], underside heating-based systems [8,9], and passive anti-icing measures by means of hydrophobic/super-hydrophobic coatings [10–14]. Glahn & Blatz [9] investigated the power requirements for IGV ice protection by using continuous and cyclical heating methods in the early 1950s. The effects of ambient air temperature, liquid water content (LWC), incoming flow velocity, heat-on-period, and cycle times on the power requirements for the two heating strategies were evaluated. It was found that a cyclical heating method can provide a total power saving as high as 79% over that of the continuous heating method. Zhu et al. [7] conducted a numerical study to investigate the impingement of water droplets and mass transfer characteristics around an icing entry strut, and the simulation results were validated against experimental data. Dong et al. [15] used a modified Lagrangian approach and a coupled algorithm to predict the characteristics of impinging water droplets and surface temperature distributions over an aero-engine inlet strut model under an icing condition. The same authors also conducted an experimental study to evaluate the performance of an anti-/de-icing system that utilizes hot lubricating oil for the icing protection of the same entry strut model in an icing tunnel [16]. The computational results were found to agree with the experimental data well in general. Dong et al. [17–19] also reported both numerical and experimental studies to evaluate the anti-/de-icing characteristics of a group of IGVs, where hot air was used to flow into air cavities and blow out from the trailing edges of the guide vanes. The performance of the hot-air-based anti-/de-icing system under various freestream temperature and LWC levels were evaluated. Ma et al. [20] and Ma & Zhang [21] developed a new concept for IGV icing protection with hot-air being exhausted from the air supply cavity to the airfoil leading edge, i.e., the exhausted hot-air would sweep off the runback surface water and impinging supercooled water droplets. More recently, Tatar and Aras [22] investigated the effects of exit angle of the discharge hole and break edge operation on the anti-/de-icing performances of a static vane model, and found that the configuration without break edge would provide higher system efficiency in icing protecting than the other compared configurations.

While hot-air-based strategy has been demonstrated to be an effective and reliable approach for IGV icing protection, such systems usually rely on utilizing bleed air taken from the airflow behind compressors, which would cause performance penalties to the aero-engines (i.e., lower engine efficiency [3], extra weight, and complexity of maintenance) or cause potential failure of the control system [23]. A good understanding of the relevant underlying physics about the unsteady heat transfer process pertinent to the icing and anti-/de-icing of IGV is essential in order to optimize the design paradigms to minimize the requirements of the bleed air for the anti-/de-icing operation, thereby, minimizing the performance penalties to the aero-engines [24]. It should be noted that, while a number of previous studies were conducted to investigate IGV icing phenomena, very little can be found in the literature to provide quantitative measurements to characterize the unsteady heat transfer during the dynamic ice formation/accretion process and to reveal the characteristics of the IGV surface temperature variations during the anti-/de-icing process.

In the present study, a comprehensive experimental investigation was conducted to quantify the important microphysical processes pertinent to IGV icing phenomena and to characterize a hot-air-based anti-/de-icing system with the ultimate goal of reducing the requirements of the bleed air for the IGV anti-/de-icing operation, thereby, minimizing the performance penalties to the aero-engines. The experimental study was performed in the icing research tunnel available at Iowa State University (i.e., ISU-IRT). A hollowed IGV model embedded with U-shaped hot-air flowing conduit was designed and manufactured for the experimental study. In addition to quantify the characteristics of the convective heat transfer over the surface of the heated IGV model, a comprehensive experimental campaign was also conducted to examine the effects of the operation parameters of the hot-air-based IGV anti-/de-icing system (i.e., by adjusting the temperature and mass flow rate of the hot-air stream) on its effectiveness for IGV icing protection. During the experiments, while a high-resolution digital imaging system was used to record the dynamic ice accretion or anti-/de-icing process over the surface of the IGV model for the test cases with and without turning on the hot-air supply system, the corresponding surface temperature distributions over the IGV model under different test conditions were also measured quantitatively by using a row of embedded thermocouples. The acquired ice accretion or anti-/de-icing images were coordinated with the quantitative surface temperature measurements to elucidate the underlying physics.

2. Experimental setup and test models

2.1. ISU-Icing research tunnel (ISU-IRT)

The experimental study was performed in the Icing Research Tunnel of Iowa State University (i.e., ISU-IRT). As shown schematically in Fig. 1, ISU-IRT is a research-grade, multifunctional icing tunnel with a transparent test section of 0.40 m × 0.40 m × 2.0 m in size. An axial fan was used to drive the airflow inside the tunnel, with the wind speed up to 60 m/s in the test section. The tunnel is refrigerated via a heat exchanger, which is chilled by a 50-kW compressor (Vilter™), to cool the airflow inside the tunnel down to −25 °C. An array of 8 pneumatic atomizing spray nozzles (Spraying Systems Co., 1/8 NPT-SU11) along with pressure regulators and flow meters were installed at the entrance of the contraction section of ISU-IRT to inject micro-sized water droplets with a median volumetric diameter (MVD) about 20 μm into the airflow. The mass flow rate of the water injected into ISU-IRT was measured directly by using a digital flow meter (Omega, FLR-1605A). By manipulating the pressure regulators on the air and water supply lines of the spray nozzles, the mass flow rate of the water droplets injected into ISU-IRT, thereby, the liquid water content (LWC) inside the icing tunnel, can be adjusted. In summary, ISU-IRT can be operated over a range of test conditions, i.e., from very dry rime ice (e.g., LWC ≈ 0.2 g/m^3) to extremely wet glaze ice (LWC > 5.0 g/m^3), to duplicate/simulate atmospheric icing phenomena over a range of icing conditions [25–30].

2.2. IGV model

An IGV model with a generalized NACA 0012 airfoil profile in the cross-section was designed and manufactured for the experimental study. As shown in Fig. 1, the IGV model, which is 152 mm in the chord length (i.e., C = 152 mm), consists of three parts along the 406 mm long span. The central part of the IGV model, which has a spanwise length of 152 mm, is hollowed and embedded with a U-shaped hot-air flow conduit to let hot air circling inside the test model for anti-/de-icing operation. The central part is made of Aluminum 6061material and manufactured by using a CNC machine. The thermal conductivity and specific heat of the Aluminum 6061material are k_{AL} = 200 W/m·K and c_{AL} = 0.897 J/g·K, respectively [31]. The other two side parts of the test model, which are made of thermoplastic material (i.e., Stratasys, ULTEM® 1010) and manufactured using a rapid prototype machine (i.e., 3-D printer), were mounted at two sides of the central part and used for supporting purpose.

In the present study, three sets of T-typed thermocouples (OMEGA®, 5TC-KK-T-20-72) with measurememnt uncertainty level of ± 0.5 °C were embedded inside the hot-air conduit of the IGV model to monitor

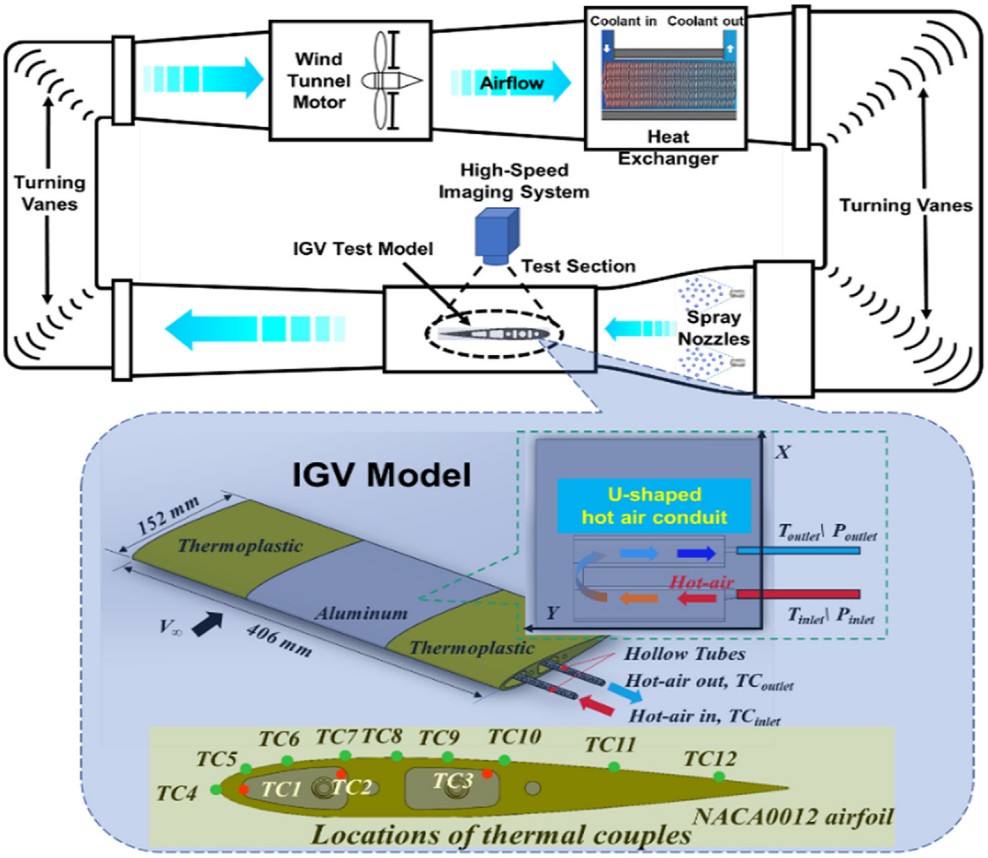

Fig. 1. A schematic of the ISU-IRT and IGV model.

Table 1
The streamwise locations of the thermocouples on the IGV model.

Thermal couples	TC#4	TC#5	TC#6	TC#7	TC#8	TC#9	TC#10	TC#11	TC#12
Streamwise location (X/C)	0	0.05	0.10	0.20	0.30	0.50	0.60	0.70	0.90

the temperatures of the hot-air stream. While the thermocouple #1 (i.e., TC#1) was embedded in the first hot-air cavity near the airfoil leading edge, the thermocouple # 2 (i.e., TC#2) was mounted at the backside of the first hot-air cavity; and the thermocouple #3 (i.e., TC#3) was embedded at the backside of the second hot-air cavity. In the meaning time, nine sets of T-typed thermocouples were flush-mounted over the surface of the IGV model with 0.064 mm thick thermocouple adhesive labels made of a polyimide film, to measure the variations of the surface temperatures during the ice accretion or anti-/de-icing process. As shown clearly in Fig. 1, the thermocouple # 4 to #12 (i.e., TC#4 ~ TC#12) were pasted on the upper surface of the IGV model from the airfoil leading edge to the trailing edge. The streamwise locations of the thermocouples over the surface of the IGV model are given in Table 1.

2.3. Hot-air supply system used in the present study

Fig. 2 shows the schematics of the hot-air supply system used for the present study, which consists of a large-scale high-pressure compressed air tank that provide dry high pressure air resource, water and particle filters, valves, air pressure regulators and flowmeters (OMEGA, FMA-2612 A, ± 0.8% accuracy), an in-line electric heater (SYLVANIA, 6 KW @ 220 V), a power unit (PAYNE Controls, Model 18DZi), a micro-controller (Fuji Electric, Model PXF4) and a number of monitoring K-type thermocouples. The system can continuously supply stable pressurized hot air at desired mass flow rates and temperatures via a feedback control module for the anti-/de-icing operation. While the main specifications of the hot-air supply system are given in Table 2, the operation profiles of the hot-air supply system are given in Fig. 3 with all the flow parameters measured at the exit of the hot-air supply system.

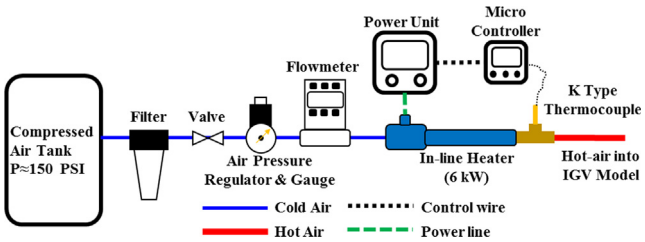

Fig. 2. The schematic of the hot-air supply system.

Table 2
The primary parameters of the hot-air supply system.

Input voltage, $U_{max,}$ (V)	220	Max input current, I_{max} (A)	27.3	Max power, P_{max} (kW)	6
Power unit efficiency, η	99%	Max flow rate, $Q_{air,max}$ (SLPM)	500	Max air pressure, $P_{air,max}$ (PSIG)	50

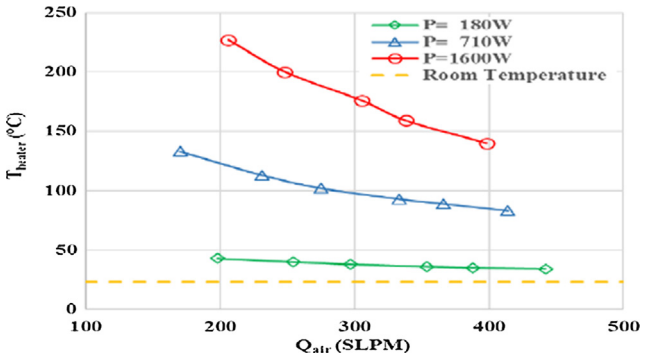

Fig. 3. The measured flow parameters at the exit of the hot-air supply system.

2.4. Measurement instrumentation

In the present study, while the IGV model was mounted at the center of the ISU-IRT test section, the hot air stream was blown in and out of the hollowed IGV model through two thermally isolated connecting tubes. During the experiments, all the thermocouples were connected to a National Instrument Compact DAQ system with a module of NI 9213 to record the temperature changes at the acquisition rate of 10 Hz . The pressure at the inlet and outlet of the hot air conduit of the IGV model was also measured by a digital pressure transducer (Scanivalve, Model DSA®3217) with ± 100 PSID pressure range and ± 0.05% in measurement accuracy.

During the experiment, a high-speed imaging system (i.e., PCO Tech, Dimax Camera, 2 K pixels × 2 K pixels in spatial resolution) along with an optical lens (Nikon, 60 mm Nikkor 2.8D) was used to record the dynamic ice accretion or anti-/de-icing process over the surface of the IGV model under different test conditions. The imaging system was positioned normal to the airfoil chord of the IGV model. A pair of 200 W Studio-LED lights (RPS Studio Light, RS-5620) were used to provide low-flicker illumination to ensure the high quality of the acquired images.

2.5. Design of the experiments and test conditions

In the present study, an experimental campaign was performed to quantify the characteristics of the unsteady heat transfer process over the surface of the IGV model, and to evaluate the effects of the operation parameters of the hot-air-based anti-/de-icing system on its effectiveness for IGV icing protection. During the experiments, the temperature and velocity of the incoming airflow inside ISU-IRT were kept at the same values (i.e., V_∞ = 40 m/s and T_∞ = −5 °C). The characteristics of the convective heat transfer process over the surface of the IGV model was investigated at first under a dry test condition. Under the dry test condition, while the hot-air stream was flowing in and out of the hollowed IGV model continuously, the water spray system of ISU-IRT was turned off. Since no supercooled water droplets are containing in the incoming airflow, no ice would accrete over the surface of the IGV model under the dry testing condition. Since the IGV model will be heated up gradually due to the continuous addition of the extra thermal energy provided by the hot-air supply system, the surface temperature of the IGV model would increase gradually until reaching a thermal steady state. After the system reaching to a thermal steady state, the temperature distributions around the IGV model would not change with time anymore, then the net thermal energy flux provided by the hot-air supply system would be dissipated/transferred out by convective heat transfer via the frozen-cold airflow over the surface of the IGV model and conductive heat transfer via the solid substrates of the supporting parts to mount the IGV model. Based on the measured surface temperature distributions, the characteristics of the convective heat transfer over the surface of the IGV model were examined/analyzed quantitatively.

After finishing the experimental studies under the dry testing condition, the water spray system of ISU-IRT was then turned on, and the supercooled water droplets carried by the frozen-cold incoming airflow would impact onto the heated surface of the IGV model for the wet testing experiments. Highly depending on the operation parameter settings of the hot-air supply system (i.e., the net thermal energy flux provided by the hot-air supply system), ice may or may not accrete over the surface of the IGV model under the wet testing conditions. In the present study, the mass flow rate and temperature of the hot-air stream flowing in and out of the hollowed IGV model were adjusted to explore/optimize the design paradigm of the hot-air-based anti-/de-icing system for a successful IGV icing protection.

3. Measurement results and discussions

3.1. Ice accretion process on the IGV model before turning on the hot-air supply system

Before starting the ice accretion or anti-/de-icing experiments, ISU-IRT was operated at a prescribed temperature level (i.e., T = −5 °C for the present study) for at least 20 min to ensure the tunnel reached a thermal steady state. Since the airflow temperature inside the ISU-IRT was well below the freezing point of water, the micro-sized water droplets exhausted from the water spray nozzles would be cooled down rapidly and become supercooled water droplets. Upon impacting onto the surface of the test model, the super-cooled water droplets would go through a phase change process (i.e., solidification process) rapidly, i.e., starting a dynamic ice accretion process, on the surface of the IGV model for the test cases without turning on the hot-air supply system.

Fig. 4 gives the typical snapshot images acquired by using the high-resolution imaging system to reveal the dynamics ice accretion process over the surface of the IGV model for the test cases without turning the hot-air supply system. It can be seen that, upon the impacting of the super-cooled water droplets carried by the frozen-cold incoming

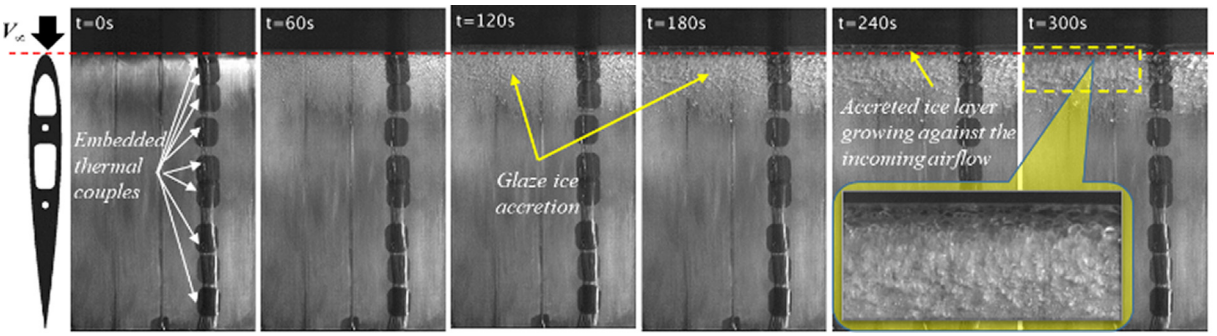

Fig. 4. Time evolution of the dynamic ice accretion process on the IGV model without turning on the hot-air-based anti-de-icing system (V_∞ = 40 m/s, T_∞ = −5 °C, LWC = 1.5 g/m^3).

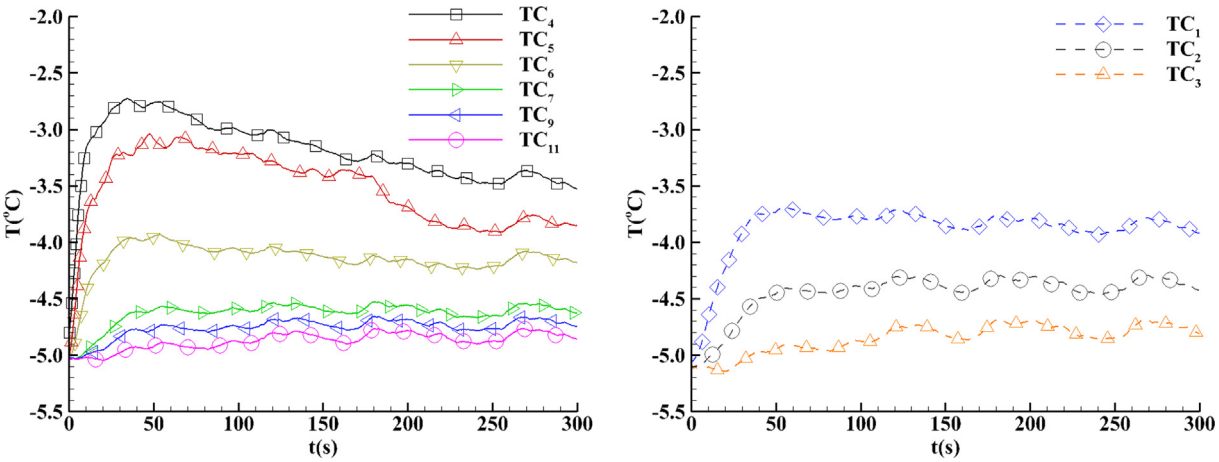

(a). Measured temperatures on the surface (b). Measured temperatures inside the IGV model

Fig. 5. The measured surface temperature profiles on the IGV model during the dynamic ice accretion process (V_∞ = 40 m/s, T_∞ = −5 °C, LWC = 1.5 g/m^3, without turning on the hot-air supply system).

airflow, ice structures were found to accrete very rapidly over the surface of the IGV model, mainly in the region near the airfoil leading edge (i.e., within the direct impingement zone of the supercooled water droplets). As shown clearly in Fig. 4, under the icing condition of V_∞ = 40 m/s, T_∞ = −5 °C, LWC = 1.5 g/m^3, ice accretion on the IGV model was found to be of a typical glaze icing process, i.e., forming transparent, glassy ice structures over the surface of the IGV model, similar as those described in Waldman and Hu [32].

Fig. 5 gives the measured temperatures on the ice accreting surface of the IGV model as a function of the time after starting the ice accretion experiment, which can be used to reveal the characteristics of the dynamic ice accretion process more quantitatively. As described in Papadakis et al. [33], the direct impingement zone of the incoming supercooled water droplets would be mainly within the first ± 10% of the chord length for a NACA0012 airfoil at the angle of attack (AOA) equals to 0 deg. Right after the water spray system of ISU-IRT was switched on (i.e., at t = 0 s), the first group of the super-cooled water droplets carried by the incoming airflow would impact onto the IGV model within a narrow region near the airfoil leading edge to start the ice accretion process. As described in Liu & Hu [29], associated with the solidification process of the impacted supercooled water droplets (i.e., icing process), tremendous amount of the latent heat of fusion would be released on the surface of the IGV model, causing the surface temperature increases near the airfoil leading edge at the intial stage of the ice accretion process (i.e., at t < 30 s), as indicated by the rapid increase of the surface temperature measured by the *TC#4* (i.e., at the airfoil leading edge of X/C = 0.0), *TC#5* (i.e., at X/C = 0.05) and *TC#6* (i.e., at X/C = 0.10). The released latent heat flux derived from the measurement results of the present study were found to be consistent with the findings reported in the previous study of Chavan et al. [34].

As described clearly in Li et al. [35], the released latent heat of fusion near the airfoil leading edge could be dissipated/carried away by heat convection, heat conduction, and radiation. Due to the relatively low temperature involved in the ice accretion or anti-/de-icing experiment, the heat transfer by radiation can be neglected for all the test cases in the present study. With the incoming airflow being frozen-cold (i.e., T_∞ = −5 °C) and having a relatively high speed (i.e., V_∞ = 40 m/s), a portion of released latent heat of fusion would be carried away rapidly by convective heat transfer via the frozen-cold airflow over the ice accreting airfoil surface. Meanwhile, due to the relatively high thermal conductivity of the Aluminum material used to make the IGV model (i.e., k_{AL} = 200 W/m·K), a portion of the released latent heat of fusion could also be dissipated quickly by heat conduction via the solid substrate of the test model. As a result, the measured surface temperatures at further downstream locations (i.e., measured by the TC#6 ~ TC#11 which are in the downstream locations far beyond the direct impingement zone of the supercooled water droplets) were also found to increase gradually after starting the dynamic ice accretion process, as shown quantitatively in Fig. 5(a). It should also be noted that, in addition to causing the temperature increase on the surface of the IGV model, the dissipation of the released latent heat of fusion by heat conduction via the solid substrate was also found to result in substantial temperature increase inside the hollowed IGV model, as revealed quantitatively from the measured temperatures inside the IGV model (i.e., *TC#1* ~ *TC#3* were embedded inside the IGV model) given in Fig. 5(b).

It can also be seen that, even though the ice accretion experiment was performed under the test condition with relatively warm ambient temperature (T_∞ = −5 °C) and a high LWC level (i.e., LWC = 1.5 g/m^3), since the latent heat of fusion released mainly in the region near the airfoil leading edges can be dissipated rapidly by both the heat convection via the incoming frozen-cold airflow and heat conduction via the substrate of the IGV model, while most of the supercooled water droplets would be frozen into ice instantly upon impacting on the IGV model, only small portion of the impacted water mass could stay in liquid phase in the region near the airfoil leading edge. Driven by the frozen-cold airflow over the airfoil surface, the unfrozen surface water would run back along the ice accreting airfoil surface and be frozen into ice eventually before it could move too far away from the airfoil leading edge, which is called as run-back ice formation. Therefore, transparent, glassy ice structures (i.e., of typical characteristics of glaze ice as described in Liu & Hu [29]) were found to accrete mainly within the region near the leading edge (within the first 10% of the airfoil surface), as shown clearly in Fig. 4.

As the ice accretion time increases, with more and more supercooled water droplets impacting onto the IGV model, the ice layer accreted over the surface of the IGV model was found to become thicker and thicker. While the accreted ice structures on the IGV model proliferated against the incoming airflow, the surface of the iced IGV model was also found to become rougher and rougher. The much rougher airfoil surface, especially the formation of the irregular-shaped ice structures near the airfoil leading edge, would cause significant disturbances to the incoming airflow around the IGV model. It will result in large-scale flow separation over the iced IGV surface, thereby, degrading the aerodynamic performance of the IGV model significantly.

It should also be noted that, as revealed clearly from the measured temperature data given in Fig. 3, the measured temperatures inside the

hollowed IGV model (i.e., measurement results of TC#1, TC#2 and TC#3 given in Fig. 5(b)) and the measured surface temperatures at the downstream locations far beyond the direct impinging zone of the supercooled water droplets (i.e., measurement results of TC#7 to TC#11 shown in Fig. 5(a)) were all found to stay at approximately constant values after about 30 s of the ice accretion experiment. It indicates that the heat transfer process around the IGV model would reach a thermal steady state after about 30 s of the ice accretion experiment.

It can also be seen that, after about 30 s of the ice accretion experiment, the measured surface temperatures near the airfoil leading edge (i.e., the measurement data of TC#4, TC# and TC#6 given in Fig. 5a) were found to decrease gradually as the ice accretion time increase. This temperature variation can be explained by the fact of the enhanced convective heat transfer process over the much rougher surface of the iced IGV model at the later stage of the icing experiment. As shown clearly in Fig. 4, the surface of the IGV model was found to become rougher and rougher as the ice accretion time increases. The irregular-shaped ice structures accreted near the airfoil leading edge would promote a fast turbulence transition of the laminar boundary layer airflow near the airfoil leading edge, which would significantly enhance the convective heat transfer over the rougher airfoil surface [36–38]. Since the released latent heat of fusion associated with the solidification of the impacted supercooled water droplets could be dissipated much faster by the enhanced convective heat transfer over the rougher airfoil surface, the surface temperatures near the airfoil leading edge (i.e., measured by the TC#4, TC#5 and TC#6) were found to decrease gradually as the ice accretion time increases.

3.2. Characterization of convective heat transfer over the surface of the IGV model under dry test conditions

In the present study, the characteristics of the convective heat transfer process over the surface of the IGV model was also investigated under dry test conditions. For the experiments under the dry test condition, while the water spray system of ISU-IRT was turned off, the hot-air supply system was switched on so that the hot-air stream would flow in and out the hollowed IGV model continually. Since no supercooled water droplets were loaded in the incoming airflow under the dry test conditions, no ice would accrete over the IGV model.

After the hot-air supply system was turned on, the IGV model will be heated up gradually due to the continuous addition of extra thermal energy provided by the hot-air stream. In the present study, while the velocity and temperature of the incoming airflow in ISU-IRT were kept at $V_\infty = 40$ m/s and $T_\infty = -5$ °C, the mass flow rate and temperature of the hot-air stream flowing through the hollowed IGV model were varied. Table 3 lists the primary parameters of the hot-air supply system used for the present study along with the measured temperatures of the hot-air stream flowing in and out of the hollowed IGV model for the experiments under the dry test conditions.

Fig. 6 shows the time evolution of the measured temperatures over the surface of the IGV model with the operation parameters of the hot-air supply system set at the same mass flow rate $\dot{m}_{\text{air}} = 4.0$ g/s and heat temperature $T_{heater} = 40$ °C and $T_{heater} = 25$ °C, respectively. It can be seen clearly that, after the hot-air supply system was turned on, the surface temperatures of the IGV model were found to increase monotonically, due to the continuous thermal energy input added by the hot-air stream to the IGV model. It can also be seen that at about 300 s after turning on the hot-air supply system, the whole system would reach a thermal steady state with the surface temperatures of the IGV model being almost unchanged as the time increases.

Table 3 also listed the corresponding temperature distributions over the surface of the IGV model measured by the thermal couples after the system reaching the thermal steady state. The characteristics of the convective heat transfer over the surface of the IGV model under the dry testing conditions can be further analyzed based on the measured surface temperature distributions along with the mass flow rate and measured temperatures of the hot-air stream flowing in and out of the IGV model.

According to the heat transfer textbook of Incropera & Dewitt [39], the thermal flux dissipated by convective heat transfer over a heated solid surface can be estimated as:

$$\dot{Q}_{conv} = \iint h_{cv,x}(T_{surface} - T_\infty)dA, \tag{1}$$

where $h_{cv,x}$ is the local convective heat transfer coefficient, T_∞ is the temperature of the incoming airflow, $T_{surface,x}$ is the local temperature on the solid surface. It should be noted that Fossen et al. [40] and Poinsatte et al. [41] conducted a series of flight and icing tunnel experiments to determine the local convective heat transfer coefficients over NACA0012 airfoil surfaces. The convective heat transfer data were presented by using a non-dimensional Frossling number based on the airfoil chord length, which is expressed as:

$$Fr = Nu/\mathrm{Re}^{0.5} = (hc/k)/(\rho Vc/\mu)^{0.5}. \tag{2}$$

Based on the extensive measurement data derived from the flight and icing tunnel experiments, Poinsatte et al. [41] reported the variations of the Frossling number as a function of the non-dimensional surface distance over a NACA0012 airfoil surface.

Since the IGV model used in the present study also has NACA0012 airfoil profile in the cross-section, the local convective heat transfer coefficients over the surface of the IGV model can be determined based on the generalized Frossling number variation profile over a NACA0012 airfoil surface as reported in Poinsatte et al. [41]. By using the measured surface temperature data as those given in Table 3, the distribution of the thermal flux dissipated by the convective heat transfer over the surface of the IGV model after the system being in the thermal steady state can be estimated quantitatively.

Fig. 7 gives the normalized local thermal flux over the surface of the IGV model as a function of the chordwise locations under different dry testing conditions. The normalized local thermal flux is defined as the ratio between the local thermal flux over the surface of the IGV model to the corresponding value at the airfoil leading edge (i.e., at X/C = 0.0), which is expressed as:

$$\Phi = [h_{c,x}\cdot(T_{surface,x} - T_\infty)]/[h_{c,0}\cdot(T_{surface,0} - T_\infty)] \tag{3}$$

It can be seen clearly that, corresponding to the strongest convective heat transfer at the stagnation point over the airfoil surface as that

Table 3
Test cases to characterize convective heat transfer under dry conditions.

	Hot-air supply system				Measured surface temperatures on the IGV model								
Case no.	$\dot{m}_{air}$ (g/s)	T_{heater} (°C)	T_{inlet} (°C)	T_{outlet} (°C)	*TC4* (°C)	*TC5* (°C)	*TC6* (°C)	*TC7* (°C)	*TC8* (°C)	*TC9* (°C)	*TC10* (°C)	*TC11* (°C)	*TC12* (°C)
Dry#1	4.0	40.0	35.1	15.9	6.1	6.4	8.2	6.5	5.3	2.4	1.1	0.8	−0.3
Dry#2		35.0	31.0	14.2	4.8	5.6	7.2	5.2	4.5	2.0	0.8	0.6	−0.4
Dry#3		30.0	27.6	13.0	4.2	4.6	5.9	4.5	3.5	1.4	0.5	0.1	−0.8
Dry#4		25.0	23.7	11.4	3.0	4.4	5.1	3.4	2.2	0.4	−0.2	−0.7	−1.6
Dry#5	3.0	30.0	26.9	12.5	1.8	2.0	2.2	1.9	1.0	−0.8	−1.0	−1.8	−2.6
Dry#6	2.0	30.0	26.5	11.8	0.6	0.8	1.0	0.6	−0.1	−1.5	−2.0	−2.4	−3.0

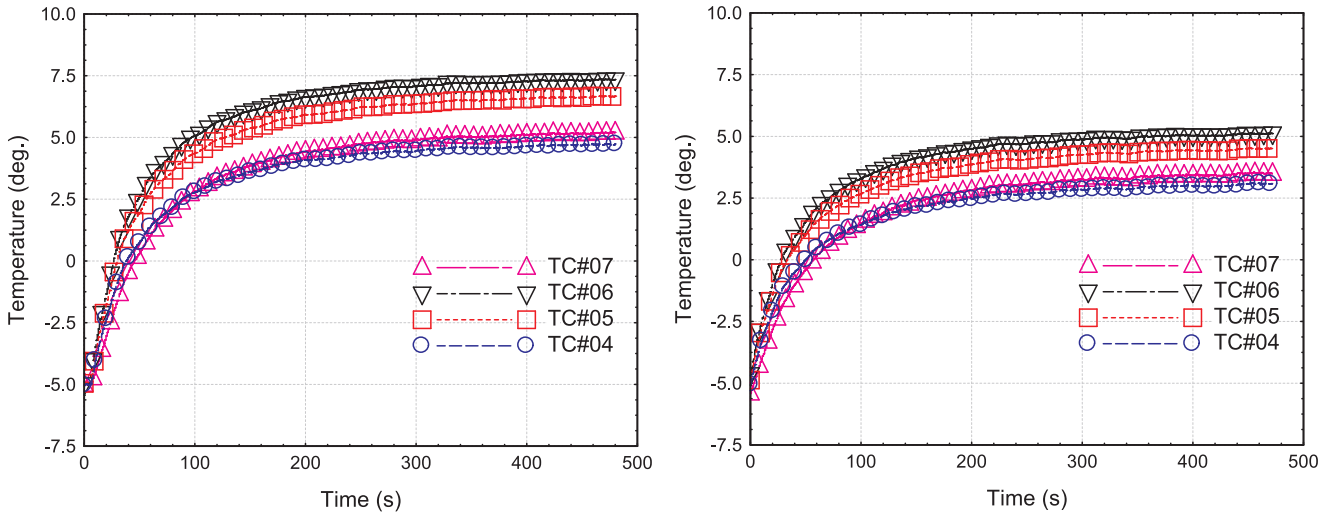

(a). Dry#1:$\dot{m}_{air}$= 4.0 g/s T_{heater}= 40 °C (b). Dry#4:$\dot{m}_{air}$= 4.0 g/s T_{heater}= 25 °C

Fig. 6. Time evolution of the measured surface temperatures on the IGV model under dry test conditions with two typical parameter settings.

reported in Yang & Hu [29], the measured local thermal flux was found to have its maximum value at the leading edge of the IGV model (i.e., also being the stagnation point when the IGV model was mounted at AOA = 0.0 deg.), as expected. The local thermal flux values (i.e., the thermal energy would be dissipated by convective heat transfer) over the surface of the IGV model were found to decrease dramatically as the chordwise location moving slightly away from the airfoil leading edge. More specifically, at the downstream location of X/C = 0.05 (i.e., at the location only slightly away from the airfoil leading edge), the local thermal flux values were found to decrease greatly and become only about 60% of the corresponding values at the airfoil leading edge. It can also be seen that, the local thermal flux values were found to have much more moderate decreasing rates at the further downstream locations, and eventually flat out at the downstream locations of X/C > 0.5 with the local thermal flux values becoming less than 20% of the corresponding values at the airfoil leading edge. Such a distribution pattern for the local thermal flux values (i.e., the rate at which the thermal energy would be dissipated by convective heat transfer) over the surface of the IGV model would indicate that the thermal energy provided by the hot-air stream to the IGV model would be dissipated mainly in the region near the airfoil leading edge via convective heat transfer process. It also suggests that, with the hot-air-based anti-/de-icing system as the one used in the present study, the thermal energy provided by the hot-air stream would be used to prevent ice formation and accretion in the region near the leading edge of the IGV model effectively.

Based on the comparison of the normalized local thermal flux profiles under different testing conditions, it can also be seen clearly that, while the operation parameters of the hot-air supply system (i.e., the heater temperature and mass flow rate of the hot-air stream) were changed dramatically during the experiments, the characteristics of the normalized thermal flux distribution over the surface of the IGV model were found to be almost identical for the different test cases. It indicates that, for a given design of the hot-air-based anti-/de-icing system, while the distribution pattern of the thermal flux over the surface of the IGV model would be affected by the external airflow conditions and the airfoil geometry of the IGV model, it would be almost independent on the operation parameters of the hot-air supply system. It should also be noted that, the normalized thermal flux data over a NACA0012 airfoil model, as reported in the previous study of Gary et al. [42,43], were also plotted in Fig. 9 for comparison. It can be seen clearly that, the measurement results of the present study were found to agree well with that reported in Gary et al. [42,43] in general.

By integrating the distribution of the local thermal flux around the

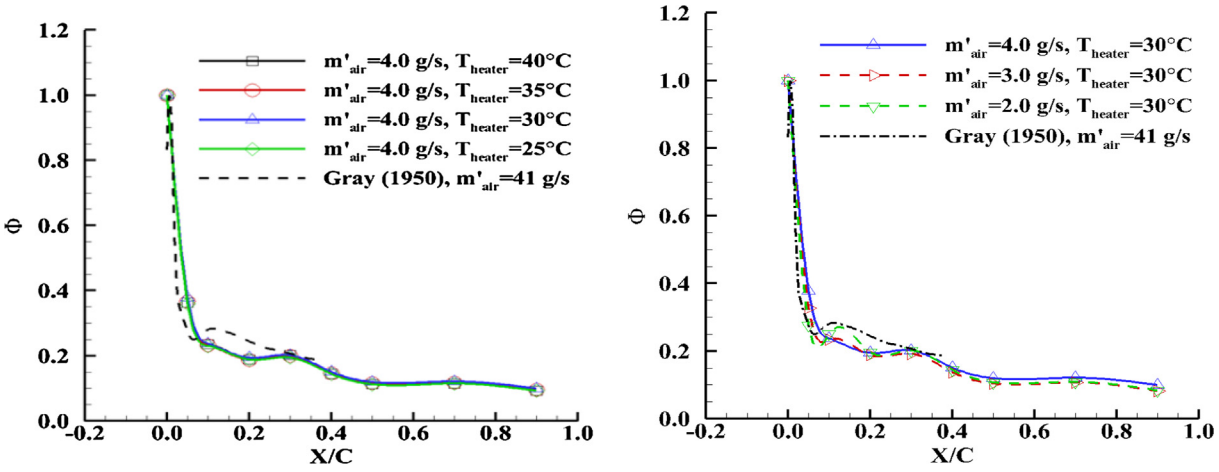

(a). Cases with different hot-air inlet temperatures (b). Cases with different hot-air flow rates

Fig. 7. Variations of local heat flux as a function of chordwise locations on the IGV model.

Table 4
Heat transfer characteristics of the hot-air-based anti-/de-icing system.

	Test case Dry #1	Test case Dry #2	Test case Dry #3	Test case Dry #4	Test case Dry #5	Test case Dry #6
Total thermal flux provided by the hot-air supply system. $\dot{Q}_{hot-air}$(W)	77.5	66.9	58.8	48.9	42.9	29.5
Integrated thermal flux dissipated by heat convection. $\dot{Q}_{conv}$(W)	65.5	57.1	50.4	42.6	37.1	25.9
Percentage of the thermal energy dissipated by convective heat transfer. $\eta \approx \dot{Q}_{conv}/\dot{Q}_{hot-air}$	85%	86%	86%	87%	86%	88%

IGV model surface, the total thermal flux dissipated by the convective heat transfer over the entire surface of the IGV model, $\dot{Q}_{conv}$, can be determined. Table 4 summarizes the integrated values of the total thermal flux dissipated by convective heat transfer over the entire surface of the IGV model for each test case. Based on the measured mass flow rate and the temperatures of the hot-air stream flowing in and out of the hollowed IGV model, the total net thermal energy flux provided by the hot-air supply system to the IGV model, $\dot{Q}_{hot-air}$, can be determined, which are also listed in Table 4 for comparison.

Based on the integrated thermal flux results listed in Table 4, it can be seen clearly that, with the experimental setup used in the present study, over 85% of the net thermal energy flux provided by the hot-air supply system to the IGV model would be dissipated by the convective heat transfer via the boundary layer airflow over the surface of the IGV model. It indicates that the majority of the thermal energy supplied by the hot-air supply system would be dissipated via the frozen-cold airflow around the IGV model, which would be used eventually for IGV icing mitigation. It should also be noted that, the difference between the total thermal energy flux provided by the hot-air supply system and the integrated thermal flux dissipated by the convective heat transfer over the surface of the IGV model, i.e., $\dot{Q}_{cond} \approx \dot{Q}_{hot-air} - \dot{Q}_{conv}$ would indicate the energy loss to be dissipated/carried away by heat conduction via the solid supporting parts to mount the IGV model.

3.3. Evaluating the effectiveness of the hot-air-based anti-/de-icing system for IGV icing mitigation

In the present study, a series of experiments were also conducted to evaluate the effects of the operation parameters of the hot-air supply system on its performance in preventing ice formation/accretion over the surface of the IGV model. During the experiments, while the airflow speed, ambient temperature and liquid water content (LWC) level in the incoming airflow were fixed at $V_\infty = 40$ m/s, $T_\infty = -5.0$ °C, and $LWC = 1.5$ g/m^3 respectively, the heater temperature and mass flow rate of the hot-air stream flowing into the hollowed IGV model, thereby, the total thermal flux provided by the hot-air supply system for the IGV anti-/de-icing operation, were adjusted in order to explore the effects of the operation parameters of the hot-air-based anti-/de-icing system on its effectiveness for IGV icing mitigation.

As described above, for the test case without turning on the hot-air supply system, upon the impact of the supercooled water droplets carried by the incoming frozen-cold airflow onto the IGV model, ice structures would accrete rapidly on the surface of the IGV model, as shown clearly in Fig. 3. However, after the hot-air supply system was turned on, the IGV model would be heated up by the hot-air stream flowing through the hollowed IGV model, causing substantial surface temperature increases of the IGV model. As a result, the dynamic ice accretion process over the surface of the IGV model was found to be changed significantly.

Fig. 8 shows the typical snapshot images acquired by the high-speed image system to reveal the anti-/de-icing process over the surface of the IGV model with the hot-air supply system operating under different test conditions. The corresponding surface temperatures measured by using the embedded thermal couples over the surface of the IGV model during the anti-/de-icing process are given in Fig. 9.

It should be noted that, for all the test cases discussed in this section, the hot-air supply system was switched on to heat up the IGV model at first to ensure the system reached a thermal steady state (i.e., the measured surface temperatures of the IGV model being almost unchanged with time). Then, the water spray system of ISU-IRT was turned on at the time of $t = 0$ s to start the anti-/de-icing experiment. Upon the impacting of the super-cooled water droplets exhausted from the water spray nozzles onto the heated IGV model, the surface temperatures of the IGV model were found to decrease monotonically, as shown quantitatively in Fig. 9. The measured surface temperatures were found to decrease very rapidly at the initial stage (i.e., for the first 25 s) of the anti-/deicing experiments, due to the unsteady heat transfer process associated with the impingement of the first group of the supper-cooled water droplets onto the heated IGV model. As the experiment goes on, while the heat transfer process over the surface of the IGV model would tend to reach to a thermal steady state gradually, the decrease rates of the surface temperatures over the IGV model were found to slow down substantially. After about 200 s of the anti-/de-icing experiment, the measured IGV surface temperatures were found to become almost unchanged with time for the rest of the experiment duration.

More specifically, for the test case shown in Fig. 8(a), the hot-air supply system was set to have $\dot{m}_{air} = 2.0$ g/s and $T_{heater} = 30$ °C (i.e., same settings as the Case Dry#6 given in Table 4). Based on the total thermal flux data listed in Table 4, about 30 Watts of the net thermal flux would be provided by the hot-air stream to heat the IGV model for the anti-/de-icing operation. The surface temperatures of the IGV model were found to increase substantially, in comparison to the baseline case (i.e., the test case without turning on the hot-air supply system). Based on the measurement results given in Table 4, the surface temperatures near the leading edge of the IGV model (i.e., measured by TC#4 ~ TC#7) were found to be above the water freezing point (i.e., $T_{wall} > 0$ °C) before having the supercooled water droplets impacting onto the IGV model. After switching on the water spray system of ISU-IRT, the supercooled water droplets carried by the incoming airflow would impact onto the IGV model, mainly in the region near the airfoil leading edge (i.e., the direct impinging zone of the supercooled water droplets, as described in Papadakis et al. [33]). As shown quantitatively in Fig. 9(a), right after the first groups of the supercooled water droplets impacted onto the IGV model, the surface temperatures near the leading edge of the IGV model (i.e., measured by TC#4 ~ TC#6) were still found to be above the freezing point of water (i.e., $T_{wall} > 0$ °C) (i.e., at the initial stage of the experiment of $t < 20$ s). It indicates that, after the impacting of the first groups of supercooled water droplets onto the heated IGV model, the impacted water mass would be heated up rapidly, and stay in the liquid phase, instead of being frozen into solid ice immediately. As a result, as shown clearly in Fig. 8(a), no ice structures were found to accrete in the region near the airfoil leading edge (i.e., within the direct impinging zone of the supercooled water droplets). Similar to that described in Zhang et al. [27], the impacted water droplets collected in the region near the airfoil leading edge would coalesce at first to form a thin film, then run back along the airfoil surface as driven by the airflow over the airfoil surface. With the water film advancing further downstream, the front contact line of the water film flow would be bugled locally, and developed into isolated water rivulets, as shown clearly in the acquired snapshot images given in Fig. 8(a).

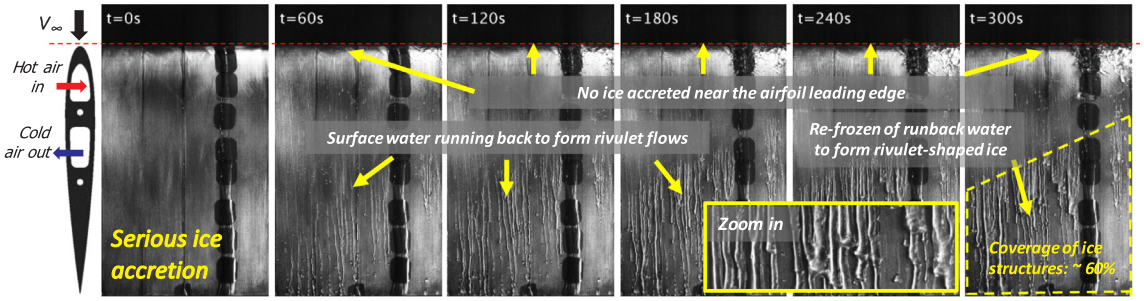

(a). The test case with $\dot{m}_{air}$ =2.0 g/s, T_{heater}= 30 ºC

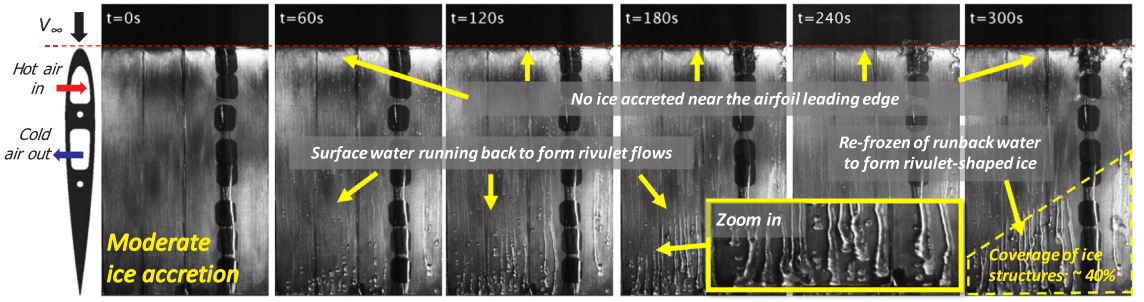

(b). The test case with $\dot{m}_{air}$ =3.0 g/s, T_{heater}= 30 ºC

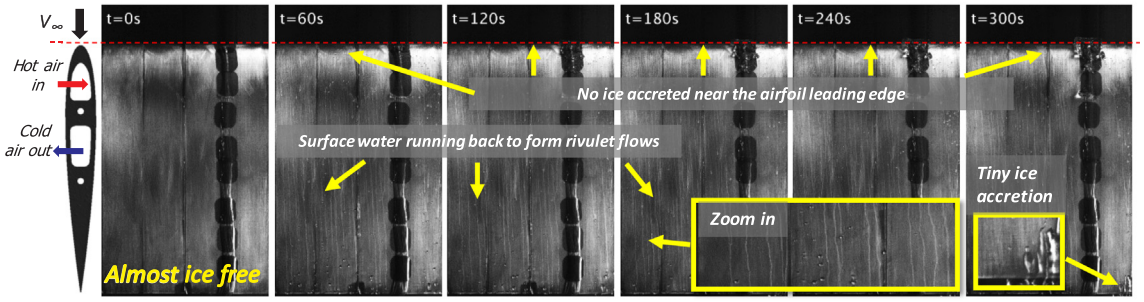

(c). The test case with $\dot{m}_{air}$ =4.0 g/s, T_{heater}= 30 ºC

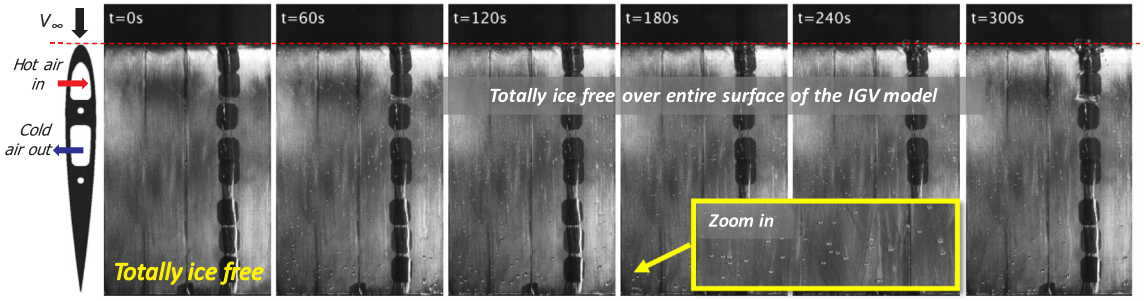

(d). The test case with $\dot{m}_{air}$ =4.0 g/s, T_{heater}= 40 ºC

Fig. 8. Time sequences of the acquired images to reveal the anti-/de-icing process on the IGV model with the hot-air supply system in different parameter settings.

Corresponding to the continuous decreasing of the surface temperature along the chordwise direction on the IGV model, the runback surface water would be cooled down gradually as moving downstream. As shown clearly in Fig. 9(a), since surface temperatures at rear portion of the IGV model (i.e., at the downstream locations to embed TC#8 ~ TC#11) were found to become lower than the water freezing point (i.e., T_{wall} < 0 ˚C), the runback water could be frozen into ice eventually at the further downstream locations. The formation of rivulet-shaped ice structures in the region near the trailing edge of the IGV model was revealed clearly in the acquired images given in Fig. 8(a).

It should be noted that, due to the continuous impingement of the supercooled water droplets onto the IGV model, the measured temperatures on the IGV model were found to decrease monotonically as the time increases until reaching a thermal steady state at about 200 s after starting the anti-/de-icing experiment. As shown clearly in the acquired snapshot images given in Fig. 8(a), corresponding to the continuous surface temperature decrease of the IGV model with the increasing time, formation of rivulet-shaped ice structures in the downstream region near the trailing edge of the IGV model was found to be more evident in the later stage of the anti-/de-icing experiment (i.e., revealed from the snapshot images taken at t > 180 s), in comparison to those formed at the earlier stage of the experiment. As shown schematically in Fig. 8(a), since the hot-air steam was designed to flow into the hollowed IGV model from the left side of the IGV model, the surface temperatures on the left side of the test model would be slightly

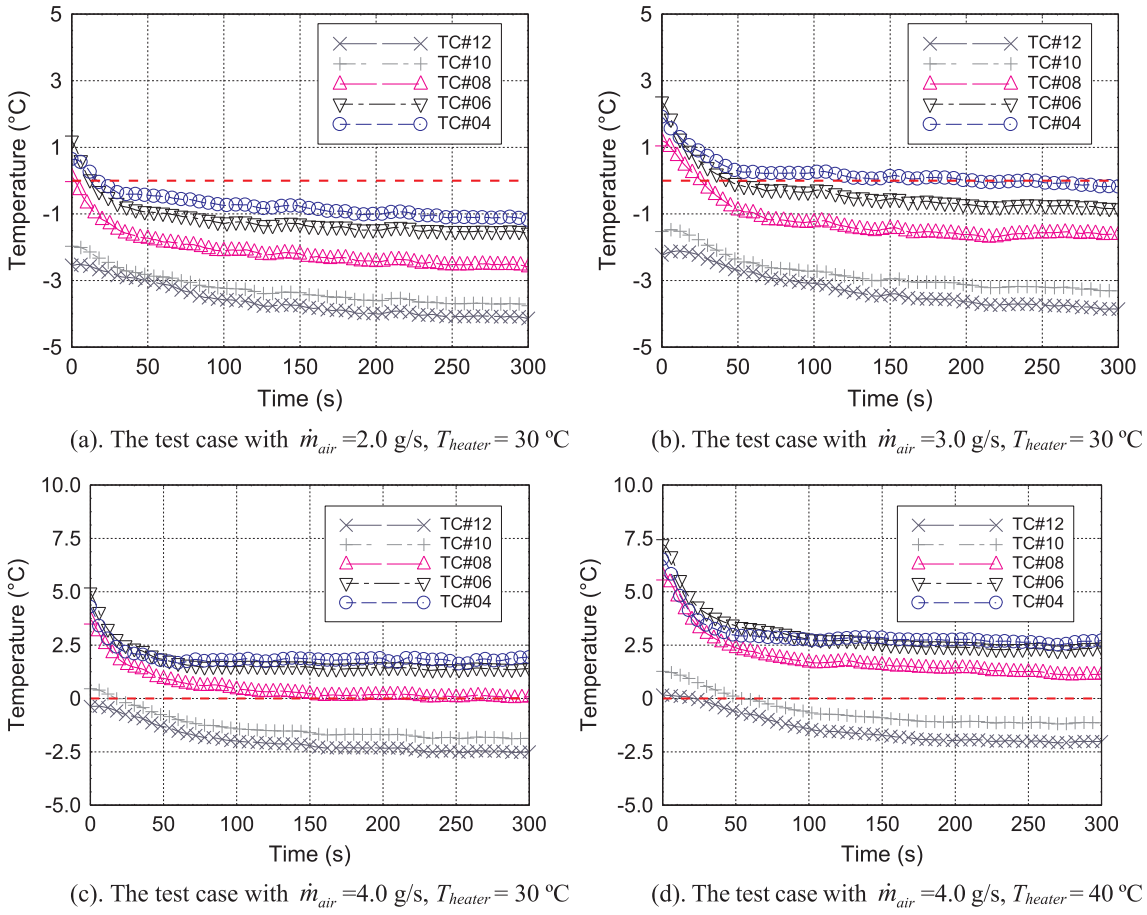

(a). The test case with $\dot{m}_{air}$ =2.0 g/s, T_{heater} = 30 ºC

(b). The test case with $\dot{m}_{air}$ =3.0 g/s, T_{heater} = 30 ºC

(c). The test case with $\dot{m}_{air}$ =4.0 g/s, T_{heater} = 30 ºC

(d). The test case with $\dot{m}_{air}$ =4.0 g/s, T_{heater} = 40 ºC

Fig. 9. The measured surface temperature on the IGV model with the hot-air supply system in different settings.

higher than those on the right side of the model. Therefore, the formation of the rivulet-shaped ice structures on the right side of the IGV model was found to occur much earlier and take place at more upstream locations, in comparison with those on the right side of the model. In summary, with the hot-air supply system operating at $\dot{m}_{air}$ = 2.0 g/s and T_{heater} = 30 °C, while the surface near the leading edge of the IGV model was found to be almost ice-free, rivulet-shaped ice structures were found to accrete over most of the downstream surface for the IGV model (i.e., ice coverage is about 60% of the airfoil surface), as indicated clearly in the image acquired at the later stage of the experiment (i.e., at t = 300 s) as given in Fig. 8(a).

In order to improve the effectiveness of the hot-air-based anti-/de-icing system for IGV icing mitigation, while the heater temperature of the hot-air supply system were still kept at T_{heater} = 30 °C, the mass flow rate of the hot-air stream was increased to $\dot{m}_{air}$ = 3.0 g/s (i.e., 50% increase in the mass flow rate of the hot-air stream). As a result, ~50% more thermal flux (i.e., ~43 W of thermal flux as the Case Dry#5 given in Table 4) would be provided by the hot-air stream to heat the IGV model for the anti-/de-icing operation. As revealed clearly in the snapshot images given in Fig. 8(b), while very similar characteristics as described above were observed on the surface of the IGV model (i.e., no ice accretion near the airfoil leading edge; formation of obvious water runback rivulets, and generation of rivulet-shaped ice structures in the further downstream region), the coverage of the ice structures in the downstream region near the trailing edge of the IGV model were found to be reduced substantially for this test case, in comparison to those of the test case with $\dot{m}_{air}$ = 2.0 g/s and T_{heater} = 30 °C.

As shown clearly in Fig. 9(b), since the hot-air supply system provided more thermal flux, majority of the surface temperatures on the IGV model, especially in the region near the airfoil leading edge (i.e., the direct impingement zone of the supercooled water droplets), were found to be well above the freezing point of water (i.e., T_{wall} > 0 °C). While rivulet-shaped ice structures were still found to accrete in the region near the trailing edge of the IGV model, the appearance of the rivulet-shaped ice structures was found to take place at much later and at much further downstream locations, in comparison to those shown in Fig. 8(a). More specifically, the area coverage of the ice formation/accretion was found to reduce to only ~40% on the rear surface of the IGV model, as shown clearly from the acquired snapshot images given in Fig. 8(b). In summary, with ~50% more thermal flux provided by the hot-air stream, the hot-air-based anti-/de-icing system was found to have a much better performance for IGV icing mitigation. However, ice structures were still found to accrete on the IGV model for this test case.

For the test case shown in Fig. 8(c), while the heater temperature of the hot-air supply system was still kept at T_{heater} = 30 °C, the mass flow rate of the hot-air stream was further increased to $\dot{m}_{air}$ = 4.0 g/s to achieve the goal of keeping the entire surface of the IGV model completely ice-free. With such operating parameters, based on power input data of the Case Dry#3 given in Table 4, the hot-air supply system would provide about 60 W of the thermal energy for IGV icing protection. As shown quantitatively in Fig. 9(c), due to the significant amount of the thermal flux provided by the hot-air stream to heat up the IGV model, most of the surface temperatures on the IGV model were found to become higher than the water freezing point (i.e., T_{wall} > 0 °C) during the entire duration of the anti-/de-icing experiment. As a result, almost no ice structures were found to form over the entire surface of the IGV model, as shown clearly in Fig. 8(c). While the impacted water mass was still found to run back over the airfoil surface, however, as driven by the same incoming airflow, the runback speed of the unfrozen water was found to increase significantly for this test case.

While runback water rivulets were still found to create isolated water transport channels over the airfoil surface, the width of the runback water rivulets was found to become much smaller. Even though the incoming airflow was still kept at the same frozen-cold temperature of $T_\infty = -5$ °C, the runback water was found to stay in the liquid phase over the airfoil surface all the time until shedding eventually from the trailing edge of the IGV model. In summary, with the hot-air supply system operating at the parameter settings of $\dot{m}_{air} = 4.0$ g/s and $T_{heater} = 30$ °C, the entire surface of the IGV model was found to be totally ice-free. It demonstrates clearly that, with the proper setting of the operating parameters, the hot-air-based anti-/de-icing system would be able to prevent ice formation/accretion on the entire surface of the IGV model successfully.

Fig. 9(d) shows the acquired typical snapshot images with the hot-air supply system operating at $\dot{m}_{air} = 3.0$ g/s and $T_{heater} = 40$ °C. With such a high-power setting (i.e., at the same parameter settings as the Case Dry#1 given in Table 4), about 78 W of the thermal flux would be provided by the hot-air supply system to the IGV model for the IGV icing protection. With such a high amount of the thermal flux supplied to the IGV model, majority of the surface temperatures of the IGV model were found to become significantly higher than the water freezing point (i.e., $T_{wall} > 0$ °C) during the entire duration of the anti-/de-icing experiment, which was shown quantitatively in Fig. 9(d). Therefore, as revealed clearly from the acquired images given in Fig. 8(d), the entire surface of the IGV model was found to be completely ice-free, as expected.

4. Conclusions

A comprehensive experimental study was conducted to quantify the dynamic icing processes over the surface of an aero-engine inlet-guide-vane (IGV) model and to characterize a hot-air-based anti-/de-icing system in order to optimize the design paradigms to reduce the requirements of the bleed air for the anti-/de-icing operation, thereby, minimizing the performance penalties to aero-engines. The experimental study was performed in the icing research tunnel available at Iowa State University (i.e., ISU-IRT) under a typical glaze icing condition (i.e., $V_\infty = 40$ m/s, $T_\infty = -5$ °C, $LWC = 1.5$ g/m^3). A hollowed IGV model embedded with U-shaped hot-air flowing conduit was designed and manufactured for the experimental investigation.

The experimental results reveal quantitatively that, for the IGV model used in the present study, a majority (≥85%) of the thermal energy provided by the hot-air stream was found to be dissipated by the convective heat transfer via the frozen-cold airflow over the surface of the IGV model for the anti-/de-icing operation, while only a small portion (< 15%) of the supplied thermal flux would be dissipated by heat conduction via the substrate of the IGV model or supporting parts. The thermal energy dissipation characteristics were found to be almost independent of the operation parameters of the hot-air supply system. It was also demonstrated clearly that, by manipulating the operation parameters of the hot-air-based system (i.e., changing the temperature and/or mass flow rate of the hot-air stream), the ice formation/accretion process over the surface of the IGV model would be affected significantly. With the supplied thermal flux being relatively low (e.g., with the temperature of the hot-air stream being lower than 30 °C and its flow rate being less than 4.0 g/s), while no ice were found to form/accrete near the airfoil leading edge, rivulet-shaped runback ice structures were found to accrete in the downstream region near the trailing edge of the IGV model. As the supplied thermal flux becoming high enough, the entire surface of the IGV model were found to stay ice free during the entire duration of the icing experiment.

In summary, it was demonstrated clearly that, the hot-air-based system would be able to effectively prevent ice formation/accretion over the entire surface of the IGV model with a proper setting of the operation parameter. While the findings derived from the present study are believed to be very helpful to gain further insight into the important microphysical processes pertinent to IGV icing phenomena, the quantitative measurement results could also be used as valued database for the validation/verification of theoretical modelling and numerical simulations for more accrete predictions of IGV icing phenomena as well as optimization of the design paradigms for better IGV icing protection, thereby, minimizing the performance penalties to aero-engines. Future researches will consider the potential effects of the thermal conductivity of the IGV model substrates on the anti-/de-icing performance. A novel anti-/de-icing strategy to leverage durable hydrophobic/ice-phobic coatings will also be explored to further reduce the requirements of the bleed air for the IGV anti-/de-icing operation, thereby, minimizing the performance penalties to the aero-engines.

Declaration of Competing Interest

The authors declared that there is no conflict of interest.

Acknowledgements

The authors want to thank Mr. Yihua Peng and Mr. Andrew Jordan of Iowa State University for their help in performing the icing experiments by using Icing Research Tunnel of Iowa State University (i.e., ISU-IRT). The research work is partially supported by Pratt & Whitney and National Science Foundation (NSF) under award numbers of CMMI-1824840 and CBET-1916380.

References

[1] J.J. Lacey, Turbine engine icing and ice detection, in: ASME 1972 Int. Gas Turbine Fluids Eng. Conf. Prod. Show, 1972, p. V001T01A006. doi: 10.1115/72-GT-6.
[2] A. Linke-Diesinger, Systems of commercial turbofan engines: an introduction to systems functions, 2008. doi: 10.1007/978-3-540-73619-6.
[3] K. Yeoman, Efficiency of a bleed air powered inlet icing protective system, in: 32nd Aerosp. Sci. Meet. Exhib., Reno, Nevada, 1994. doi: 10.2514/6.1994-717.
[4] T.G. Keith, D. Witt, J. Kenneth, J.K. Nathman, D.A. Dietrich, K.M. Al-Khalil, Thermal analysis of engine inlet anti-icing systems, J. Propuls. Power 6 (1989) 628–634, https://doi.org/10.2514/3.23264.
[5] W.M. Schulze, Aircraft Engine Inlet Cowl Anti-icing System, US005088277A, 1988. < https://patentimages.storage.googleapis.com/68/44/ae/a6a6e6549cc373/US5088277.pdf > (accessed March 9, 2018).
[6] W. Lian, Y. Xuan, Experimental investigation on a novel aero-engine nose cone anti-icing system, Appl. Therm. Eng. 121 (2017) 1011–1021, https://doi.org/10.1016/j.applthermaleng.2017.04.160.
[7] Z. Jian-Jun, D. Wei, C. Ying-Lei, Numerical Study of water droplets' heat and mass transfer characteristics in an entry Strut's icing test, in: Proc. ASME Turbo Expo 2012, ASME, Copenhagen, Denmark, 2012, pp. 1–8.
[8] E. Tetteh, S.J. Stebbins, W. Spivey, E. Loth, J. Jacobs, Heat pad effects on inlet guide vane ice accretion, in: 15th Int. Energy Convers. Eng. Conf., 2017. doi: 10.2514/6.2017-4783.
[9] U. Von Glahn, R.E. Blatz, Investigation of Power Requirements for Ice Prevention and Cyclical De-Icing of Inlet Guide Vanes with Internal Electric Heaters, Cleveland, Ohio, 1950. < https://ntrs.nasa.gov/archive/nasa/casi.ntrs.nasa.gov/19810068707.pdf > (accessed March 9, 2018).
[10] K.D. Esmeryan, C.E. Castano, R. Mohammadi, Y. Lazarov, E.I. Radeva, Delayed condensation and frost formation on superhydrophobic carbon soot coatings by controlling the presence of hydrophilic active sites, J. Phys. D. Appl. Phys. 51 (2018), https://doi.org/10.1088/1361-6463/aaa188.
[11] K.D. Esmeryan, A.H. Bressler, C.E. Castano, C.P. Fergusson, R. Mohammadi, Rational strategy for the atmospheric icing prevention based on chemically functionalized carbon soot coatings, Appl. Surf. Sci. 390 (2016) 452–460, https://doi.org/10.1016/j.apsusc.2016.08.101.
[12] M. Zheng, Z. Guo, W. Dong, X. Guo, Experimental investigation on ice accretion on a rotating aero-engine spinner with hydrophobic coating, Int. J. Heat Mass Transf. (2019) 404–414, https://doi.org/10.1016/j.ijheatmasstransfer.2019.02.104.
[13] P. Kim, T.S. Wong, J. Alvarenga, M.J. Kreder, W.E. Adorno-Martinez, J. Aizenberg, Liquid-infused nanostructured surfaces with extreme anti-ice and anti-frost performance, ACS Nano 6 (2012) 6569–6577, https://doi.org/10.1021/nn302310q.
[14] L. Cao, A.K. Jones, V.K. Sikka, J. Wu, D. Gao, Anti-icing superhydrophobic coatings, Langmuir 25 (2009) 12444–12448, https://doi.org/10.1021/la902882b.
[15] W. Dong, J. Zhu, Z. Zhou, X. Chi, Heat transfer and temperature analysis of an aeroengine strut under icing conditions, J. Aircr. 52 (2015) 216–225, https://doi.org/10.2514/1.C032107.
[16] W. Dong, J. Zhu, Z. Zhou, X. Chi, Heat transfer and temperature analysis of an anti-icing system for an aero-engine strut under icing condition, in: 43rd AIAA Thermophys. Conf., 2012, pp. 2012–2753. doi: 10.2514/6.2012-2753.
[17] W. Dong, J.J. Zhu, Q.Y. Zhao, Numerical simulation analysis of a guide vane hot air anti-icing system, in: 42nd AIAA Thermophys. Conf., 2011, pp. 1–10. doi: 10.2514/

6.2011-3944.
[18] W. Dong, J. Zhu, M. Zheng, G.L. Lei, Z.X. Zhou, Experimental study on icing and anti-icing characteristics of engine inlet guide vanes, J. Propuls. Power. 31 (2015) 1330–1337, https://doi.org/10.2514/1.B35679.
[19] W. Dong, J. Zhu, G. Lei, M. Zheng, Numerical simulation of hot air anti-icing charateristics of an aero-engine strut, 53rd AIAA Aerosp. Sci. Meet. 2015, pp. 1–13, , https://doi.org/10.2514/6.2015-0537.
[20] H. Ma, W. Chen, D. Zhang, Numerical investigation of engine inlet vane hot–air anti–icing system with surface air film, Int. J. Mod. Phys. Conf. Ser. 19 (2012) 331–340, https://doi.org/10.1142/S2010194512008926.
[21] H. Ma, D. Zhang, Experiment investigation of hot-air anti-icing structure of engine inlet vane, 2016 IEEE/CSAA Int. Conf. Aircr. Util. Syst. 2016, pp. 284–289.
[22] V. Tatar, H. Aras, An investigation on an anti-ice static vane of a gas turbine engine, Appl. Therm. Eng. 110 (2017) 1039–1050, https://doi.org/10.1016/j.applthermaleng.2016.09.022.
[23] F. Zhang, W. Deng, H. Nan, L. Zhang, Z. Huang, Reliability analysis of bleed air anti-icing system based on subset simulation method, Appl. Therm. Eng. 115 (2017) 17–21, https://doi.org/10.1016/j.applthermaleng.2016.11.202.
[24] T. Xie, J. Dong, H. Chen, Y. Jiang, Y. Yao, Experimental investigation of deicing characteristics using hot air as heat source, Appl. Therm. Eng. 107 (2016) 681–688, https://doi.org/10.1016/j.applthermaleng.2016.05.162.
[25] Y. Liu, K. Zhang, H. Hu, An experimental investigation on the water runback process over an airfoil surface with realistic ice roughness, in: 8th AIAA Atmos. Sp. Environ. Conf., American Institute of Aeronautics and Astronautics, Reston, Virginia, 2016. doi: 10.2514/6.2016-3140.
[26] Y. Liu, H. Hu, An experimental investigation on the convective heat transfer process over an ice roughened airfoil, in: 54th AIAA Aerosp. Sci. Meet., 2016, pp. 1–31. doi: 10.2514/6.2016-1978.
[27] K. Zhang, T. Wei, H. Hu, An experimental investigation on the surface water transport process over an airfoil by using a digital image projection technique, Exp. Fluids. 56 (2015) 173, https://doi.org/10.1007/s00348-015-2046-z.
[28] L. Gao, Y. Liu, L. Ma, H. Hu, A hybrid strategy combining minimized leading-edge electric-heating and superhydro-/ice-phobic surface coating for wind turbine icing mitigation, Renew. Energy. 140 (2019) 943–956, https://doi.org/10.1016/J.RENENE.2019.03.112.
[29] Y. Liu, H. Hu, An experimental investigation on the unsteady heat transfer process over an ice accreting airfoil surface, Int. J. Heat Mass Transf. 122 (2018) 707–718, https://doi.org/10.1016/j.ijheatmasstransfer.2018.02.023.
[30] L. Gao, Y. Liu, W. Zhou, H. Hu, An experimental study on the aerodynamic performance degradation of a wind turbine blade model induced by ice accretion process, Renew. Energy 133 (2019) 663–675, https://doi.org/10.1016/j.renene.2018.10.032.
[31] Properties of Wrought Aluminum and Aluminum Alloys, in: ASM Handbook, Vol. 2 Prop. Sel. Nonferrous Alloy. Spec. Mater., 1990, pp. 62–122. doi: 10.1361/asmhba0001060.
[32] R.M. Waldman, H. Hu, High-speed imaging to quantify transient ice accretion process over an airfoil, J. Aircr. 53 (2016) 369–377, https://doi.org/10.2514/1.C033367.
[33] M. Papadakis, R. Elangonan, G.A. Freund, M. Breer, G.W. Zumwalt, L. Whitmer, An Experimental Method for Measuring Water Droplet Impingement Efficiency on Two- and Three-Dimensional Bodies, 1989.
[34] S. Chavan, D. Park, N. Singla, P. Sokalski, K. Boyina, N. Miljkovic, Effect of latent heat released by freezing droplets during frost wave propagation, Langmuir 34 (2018) 6636–6644, https://doi.org/10.1021/acs.langmuir.8b00916.
[35] L. Li, Y. Liu, Z. Zhang, H. Hu, Effects of thermal conductivity of airframe substrate on the dynamic ice accretion process pertinent to UAS inflight icing phenomena, Int. J. Heat Mass Transf. 131 (2019) 1184–1195, https://doi.org/10.1016/J.IJHEATMASSTRANSFER.2018.11.132.
[36] N. Dukhan, G.J. Van Fossen, K.C. Masiulaniec, K.J. Dewitt, Convective heat transfer coefficients from various types of ice roughened surfaces in parallel and accelerating flow, in: 34th Aerosp. Sci. Meet. Exhib., American Institute of Aeronautics and Astronautics Inc, AIAA, 1996. doi: 10.2514/6.1996-867.
[37] R.C. Henry, D. Guffond, F. Garnier, A. Bouveret, Heat transfer coefficient measurement on iced airfoil in small icing wind tunnel, J. Thermophys. Heat Transf. 14 (2000) 348–354, https://doi.org/10.2514/2.6551.
[38] Y. Liu, K. Zhang, W. Tian, H. Hu, An experimental investigation on the dynamic ice accretion and unsteady heat transfer over an airfoil surface with embedded initial ice roughness, Int. J. Heat Mass Transf. 146 (2020) 118900, , https://doi.org/10.1016/j.ijheatmasstransfer.2019.118900.
[39] F. Incropera, D. Dewitt, Introduction to Heat Transfer, John WHey Sons, New York, NY, 1996.
[40] V. Fossen, G. James, D. Witt, J. Kenneth, J.E. Newton, P.E. Poinsatte, Measurement of local convective heat transfer coefficients from a smooth and roughened NACA-0012 airfoil – flight test data, 1988. doi: 10.2514/6.1988-287.
[41] P. Poinsatte, G. Van Fossen, K. Dewitt, Convective heat transfer measurements from a NACA 0012 airfoil in flight and in the NASA Lewis Icing Research Tunnel, 1990. doi: 10.2514/6.1990-199.
[42] V.H. Gray, D.T. Bowden, Icing Characteristics and Anti-icing Heat Requirements for Hollow and Internally Modified Gas-heated Inlet Guide Vanes, Washington, 1950. < https://ntrs.nasa.gov/search.jsp?R=19810068630 > (accessed November 20, 2018).
[43] V.H. Gray, Improvements in Heat Transfer for Anti-Icing of Gas-Heated Airfoils with Internal Fins and Partitions, Washington, 1950. < https://ntrs.nasa.gov/search.jsp?R=19810068608 > (accessed November 20, 2018).